Electronic Supplementary Information

Solid Solution Reinforced $V_3CrC_3T_x$ MXene Cathodes for Zn-Ion Micro-Supercapacitors with High Areal Energy Density and Superior Flexibility

Haoran Wang,[a] Yaqing Xue,[a] Xin Song,[a] Shulai Lei,[b,e,g] Hong Yu,[a] Cheng-Feng Du, *[a] Zewei Ren,[c] Ruisheng Guo *[a,f] and Feng Zhou[a,d,f]

[a.] State Key Laboratory of Solidification Processing, Center of Advanced Lubrication and Seal Materials, School of Materials Science and Engineering, Northwestern Polytechnical University, Xi'an 710072, China

E-mail: cfdu@nwpu.edu.cn; guoruisheng@nwpu.edu.cn

[b.] Hubei Key Laboratory of Low Dimensional Optoelectronic Materials and Devices, Hubei University of Arts and Science, Xiangyang 441053, China

[c.] School of Advanced Materials and Nanotechnology, Academy of Advanced Interdisciplinary Research, Xidian University, Xi'an, 710126, P. R. China

[d.] State Key Laboratory of Solid Lubrication, Lanzhou Institute of Chemical Physics, Chinese of Academy of Sciences, Lanzhou 730000, China

[e.] Institute of Chemistry, Free University of Berlin, Arnimallee 22, Berlin D-14195, Germany

[f.] Shandong Laboratory of Yantai Advanced Materials and Green Manufacture, Yantai 264006, China

[g.] Hubei Longzhong Laboratory, Xiangyang 441000, Hubei, China

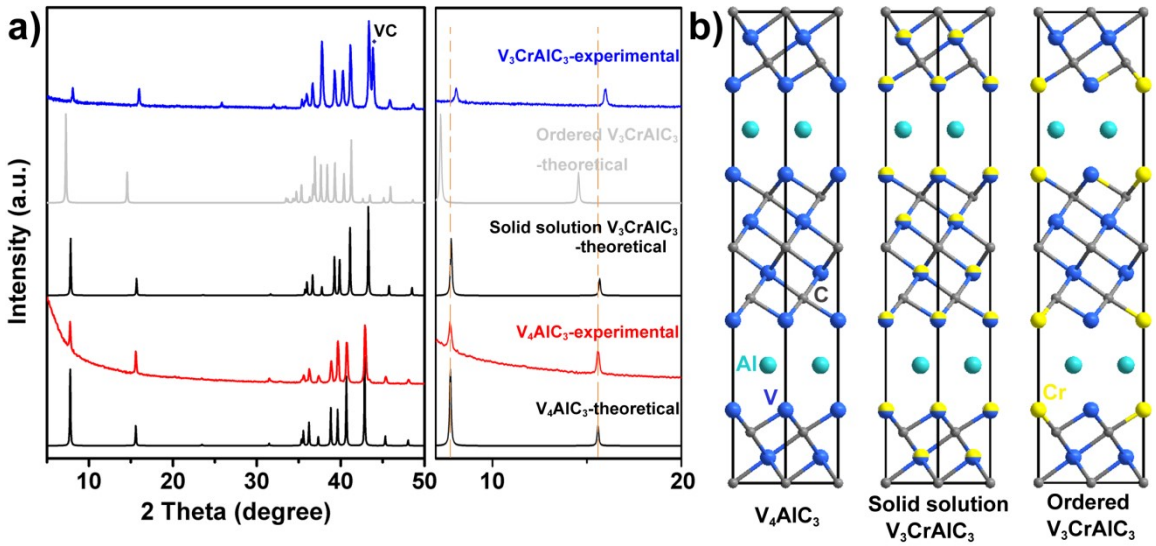

Fig. S1 a) XRD patterns of the experimental and theoretical MAX phase of V_4AlC_3 and V_3CrAlC_3; b) the simulated structure model for V_4AlC_3, solid solution V_3CrAlC_3 and ordered V_3CrAlC_3.

Based on the existing crystal structure of V_4AlC_3, two types of derived V_3CrAlC_3 MAX structures were investigated (ordered and solid solution V_3CrAlC_3), and their theoretical XRD patterns were simulated and compared with the experimental data. It can be seen that when Cr replacement is ordered distribution, the crystal plane group of {002} should shift to low angle, when Cr is solid solution distribution, the crystal plane group of {002} should shift to high angle. Compared with the XRD patterns of V_3CrAlC_3 MAX obtained from the experiment, the crystal plane group of {002} shifts to a high angle, which is more consistent with the solid solution state. Besides, the positions of the other crystal plane diffraction peaks are also consistent well with the simulated XRD patterns of the solid solution state. Therefore, it can be confirmed that Cr is present in the form of solid solution entered the V_3CrAlC_3 lattice.

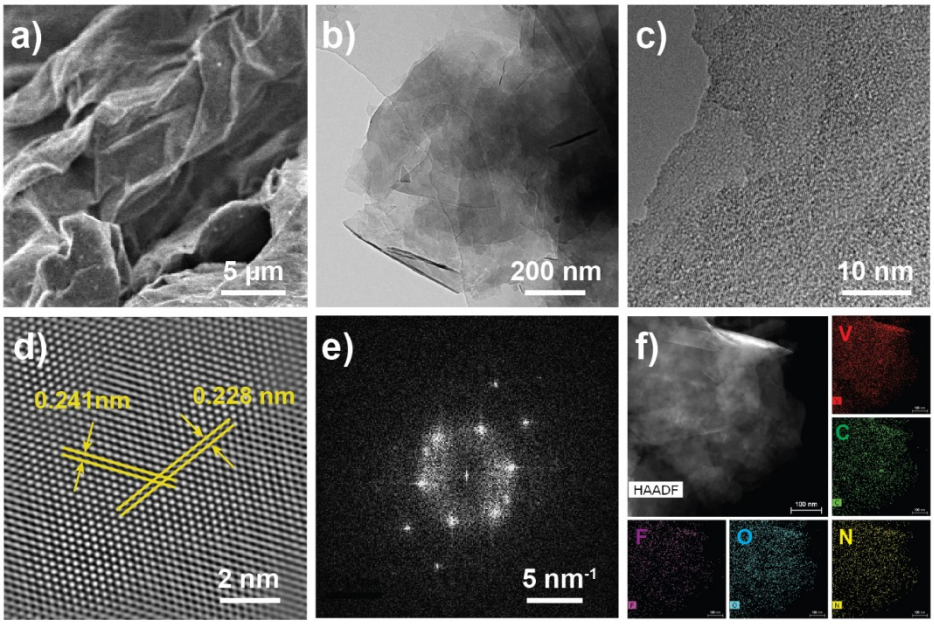

Fig. S2 a) SEM image of the purified $V_4C_3T_x$ MXene; b) TEM image and c) HRTEM image of the monolayer $V_4C_3T_x$ MXene; d) the inverse FFT image of $V_4C_3T_x$ MXene; e) HAADF-SAED of $V_4C_3T_x$ MXene; f) HAADF-STEM and the EDX elemental mapping of $V_4C_3T_x$ MXene.

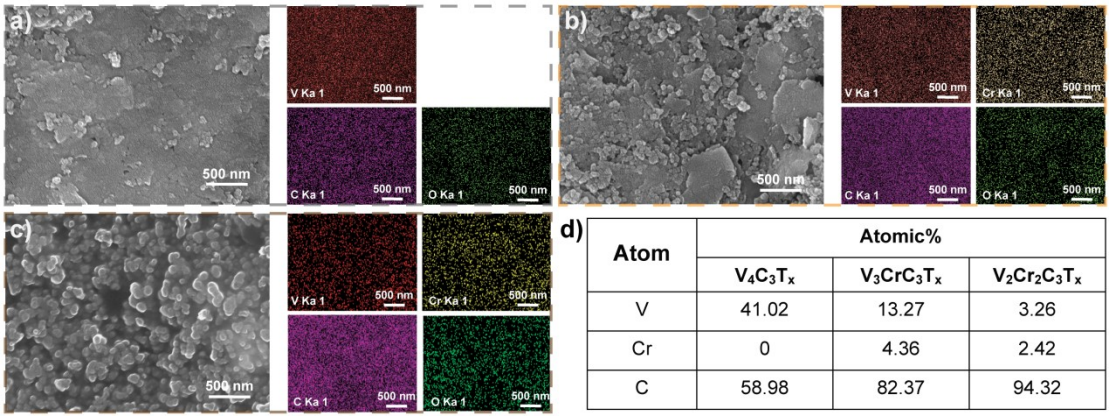

d)

Atom	Atomic%		
	$V_4C_3T_x$	$V_3CrC_3T_x$	$V_2Cr_2C_3T_x$
V	41.02	13.27	3.26
Cr	0	4.36	2.42
C	58.98	82.37	94.32

Fig. S3 SEM images of the electrode and EDX elemental mapping: a) $V_4C_3T_x$, b) $V_3CrC_3T_x$, and c) $V_2Cr_2C_3T_x$; d) the measured element ratio of $V_4C_3T_x$, $V_3CrC_3T_x$, and $V_2Cr_2C_3T_x$, respectively.

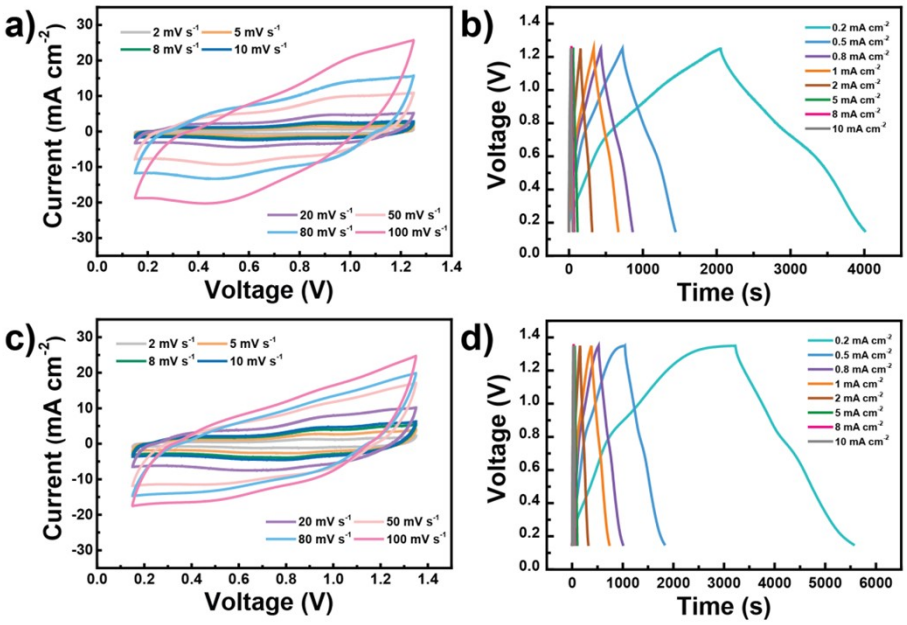

Fig. S4 CV curves and GCD profiles of a-b) Zn//$V_4C_3T_x$ SCs and c-d) Zn//$V_2Cr_2C_3T_x$ SCs.

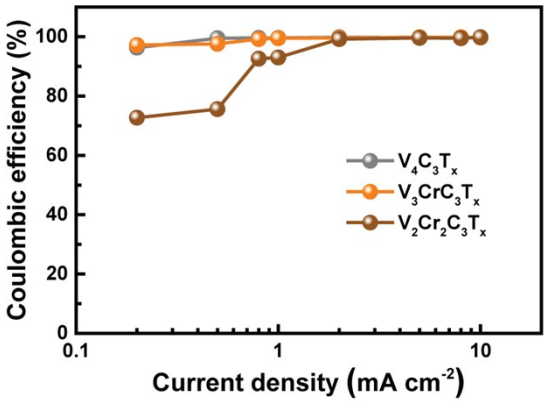

Fig. S5 *The coulombic efficiency of Zn//$V_4C_3T_x$, Zn//$V_3CrC_3T_x$ and Zn//$V_2Cr_2C_3T_x$ SCs.*

After 50000 cycles, solid solution $V_3CrC_3T_x$ cathode retains its pronounced (002) peak at around 5.5°. Besides, the original wrinkled surface and 3D porous structure are kept well. And the oxidation states of V and Cr do not change significantly, O still exists mainly in the form of M-OH, which directly proves the excellent long-term chemical stability of the solid solution $V_3CrC_3T_x$ MXene.

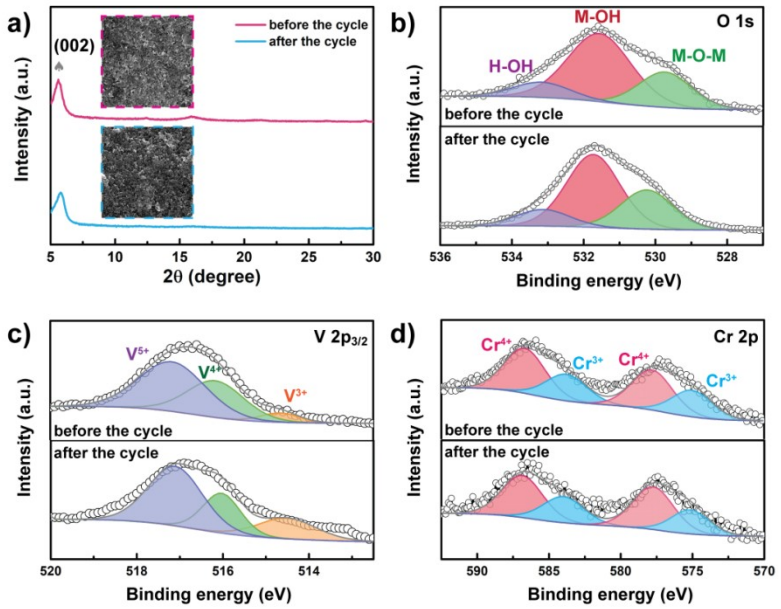

Fig. S6 Stability characterization for $V_3CrC_3T_x$ MXene cathode. a) XRD patterns and SEM images of $V_3CrC_3T_x$ MXene cathode before and after 50000 cycles. XPS spectra of the $V_3CrC_3T_x$ MXene cathode before and after 50000 cycles: b) O 1s, c) V $2p_{3/2}$, and d) Cr 2p.

After 50000 cycles, the charge-transfer resistance (R_{ct}) is bigger than that of the devices before long-term cycle test. The large resistance of the devices can be described to the formation of a thicker layer of the insulating ZSH phase on the electrode surface and sluggish intercalation of Zn^{2+}.

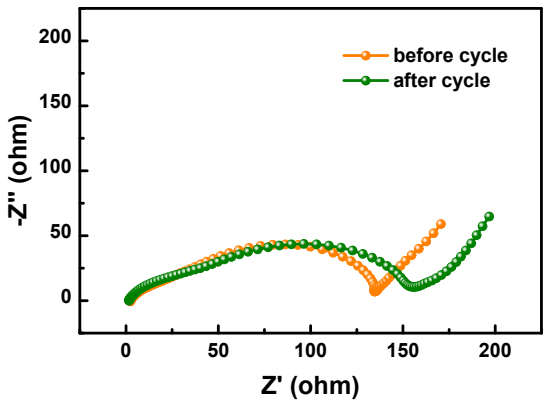

Fig. S7 The EIS before and after the long-term cycle test.

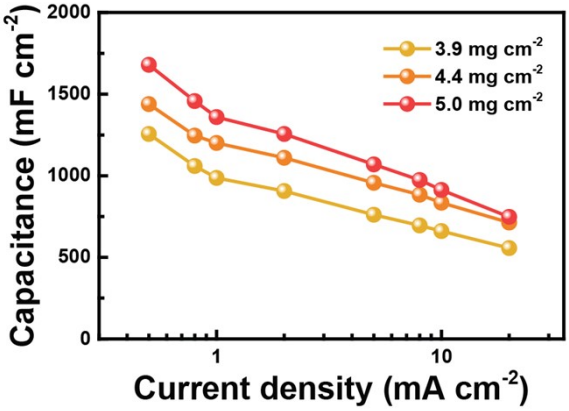

Fig. S8 The rate performances of varied mass loading of $V_3CrC_3T_x$ MXene in Zn//$V_3CrC_3T_x$ SCs.

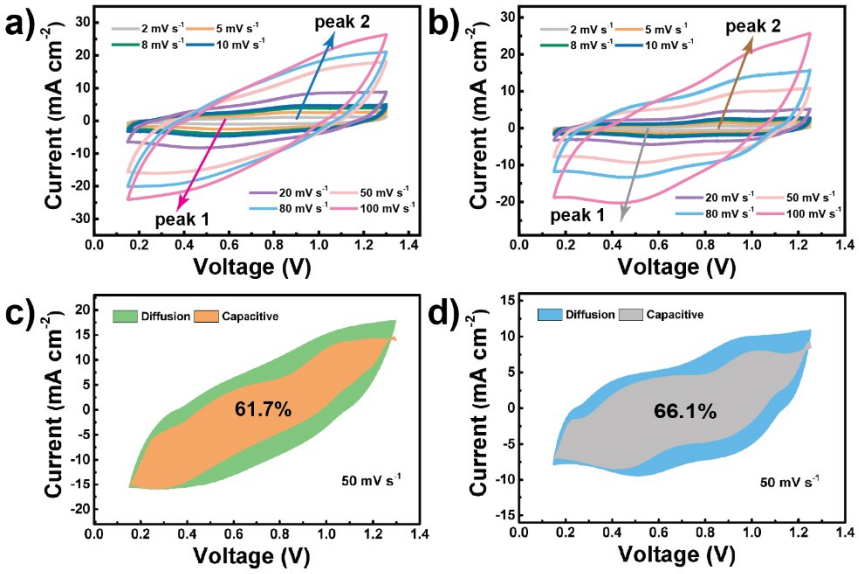

Fig. S9 CV curves measured at different scan rates (2 to 100 mV s^{-1}) of a) Zn//$V_3CrC_3T_x$ and b) Zn//$V_4C_3T_x$ SCs, respectively; the separated capacitive current and diffusion current of c) Zn//$V_3CrC_3T_x$ and d) Zn//$V_4C_3T_x$ SCs, respectively.

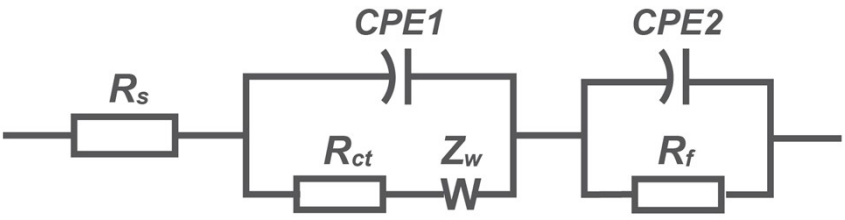

Fig. S10 Equivalent circuit fitted to the Nyquist plot.

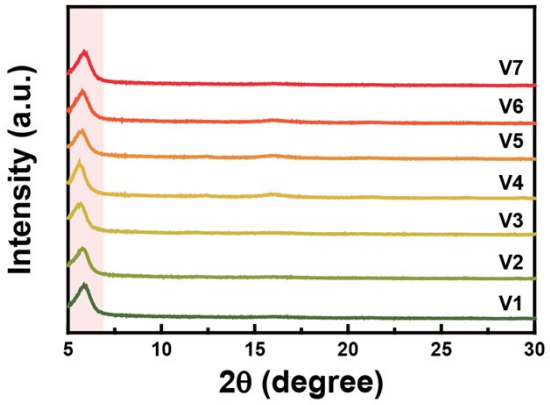

Fig. S11 Ex-situ XRD full patterns of the $V_3CrC_3T_x$ MXene cathode during the GCD process.

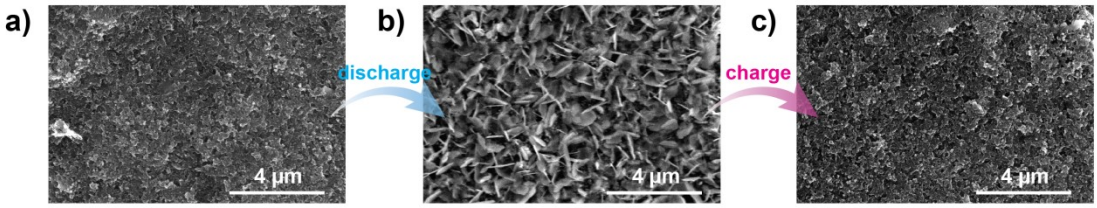

Fig. S12 SEM images of $V_3CrC_3T_x$ MXene cathode during charge/discharge process: a) pristine; b) full discharge; c) full charge.

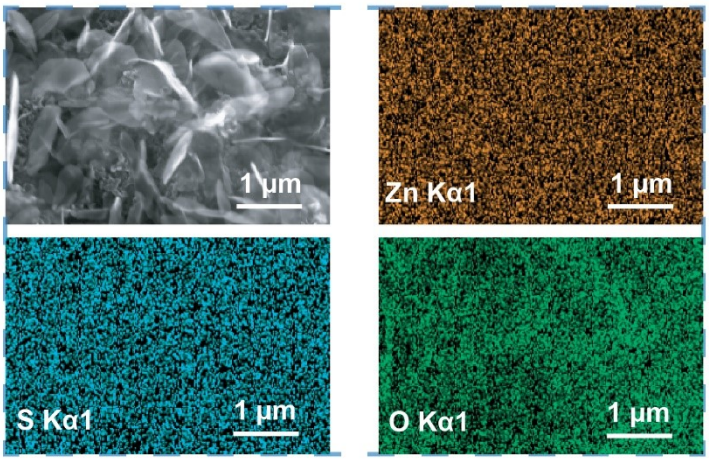

Fig. S13 EDX elemental mapping of ZSH phase.

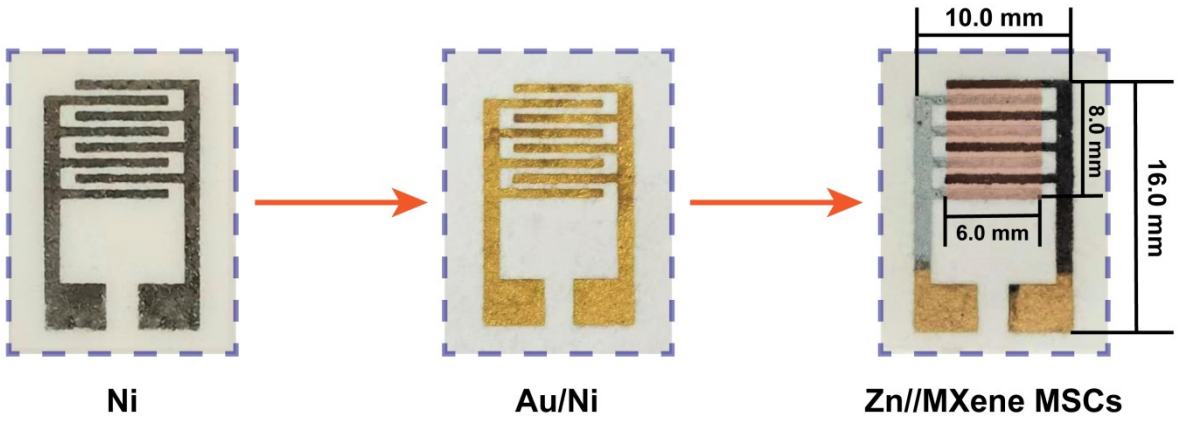

Fig. S14 Digital images of Ni patterns on paper, Au/Ni patterns on paper, and electrode materials (Zn on left side and MXene on right side) on Au/Ni interdigited current collectors, respectively.

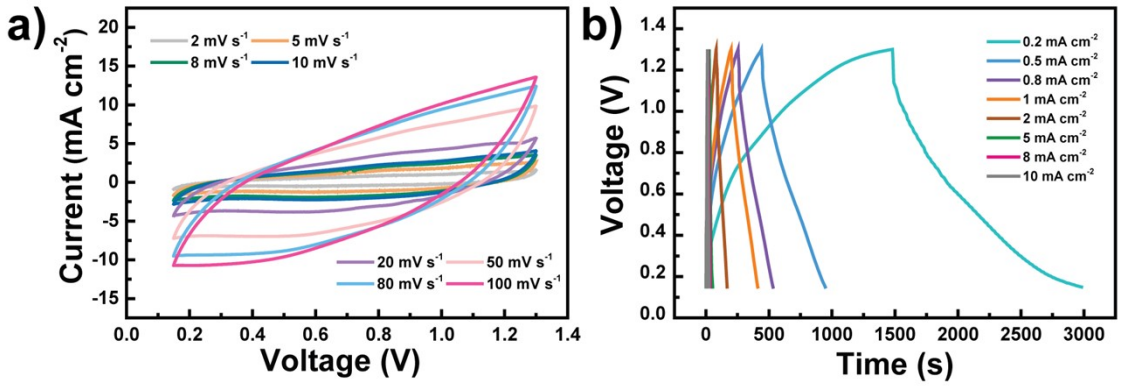

Fig. S15 a) CV curves (scan rates, from 2 to 100 mV s^{-1}) and b) GCD curves (from 0.2 to 10 mA cm^{-2}) of flexible Zn//$V_3CrC_3T_x$ MSCs.

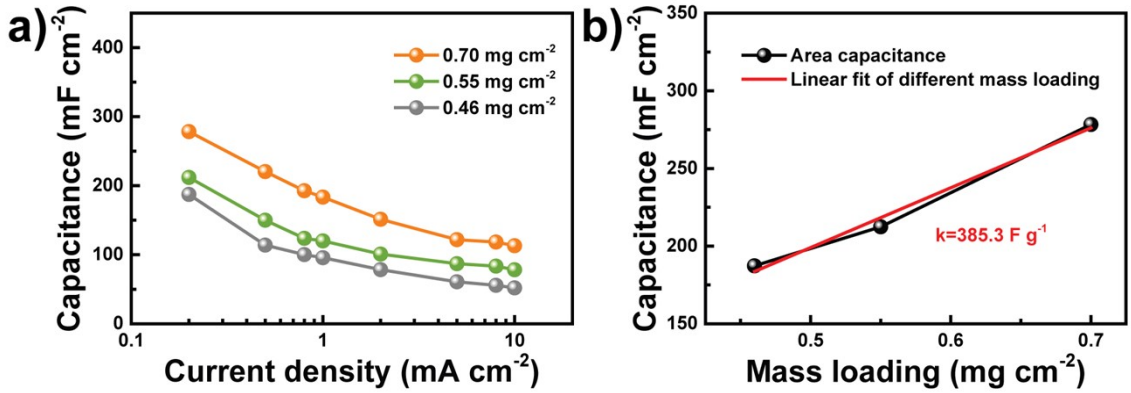

Fig. S16 a) The rate performances of varied mass loading of $V_3CrC_3T_x$ MXene in flexible Zn//$V_3CrC_3T_x$ MSCs. b) Linear fit between area capacitance and mass loading.

Obviously, compared the detailed rate performance of varied mass loading (0.46, 0.55 and 0.70 mg cm^{-2}) flexible Zn//$V_3CrC_3T_x$ MSCs (**Fig. S16a**), the greatest area capacitance can reach up to 278.3 mF cm^{-2} with the mass loading at 0.70 mg cm^{-2}, which is nearly the best area capacitance compared with reported inplane MSCs. It is presented a good positive linear correlation between area capacitance and mass loading (**Fig. S16b**), the slope *k* after the linear fit calculated as 385.3 F g^{-1} which is identical well with the specific capacity (397.5 F g^{-1}) obtained by previous electrochemical test using coin-type batteries. So, the flexible Zn//$V_3CrC_3T_x$ MSCs still shows excellent area energy density (calculated as 51.12 μWh cm^{-2}), outperforming the reported inplane flexible MSCs.

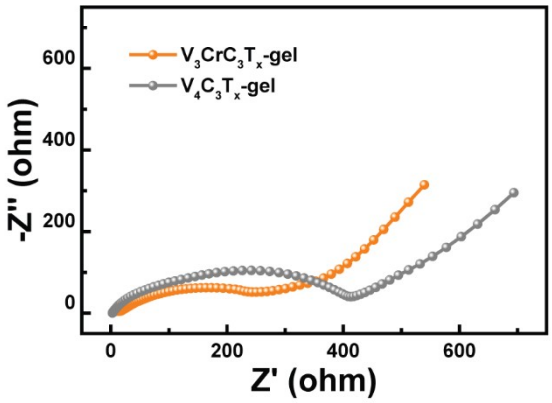

Fig. S17 EIS profile comparison between flexible Zn//$V_4C_3T_x$ and Zn//$V_3CrC_3T_x$ MSCs.

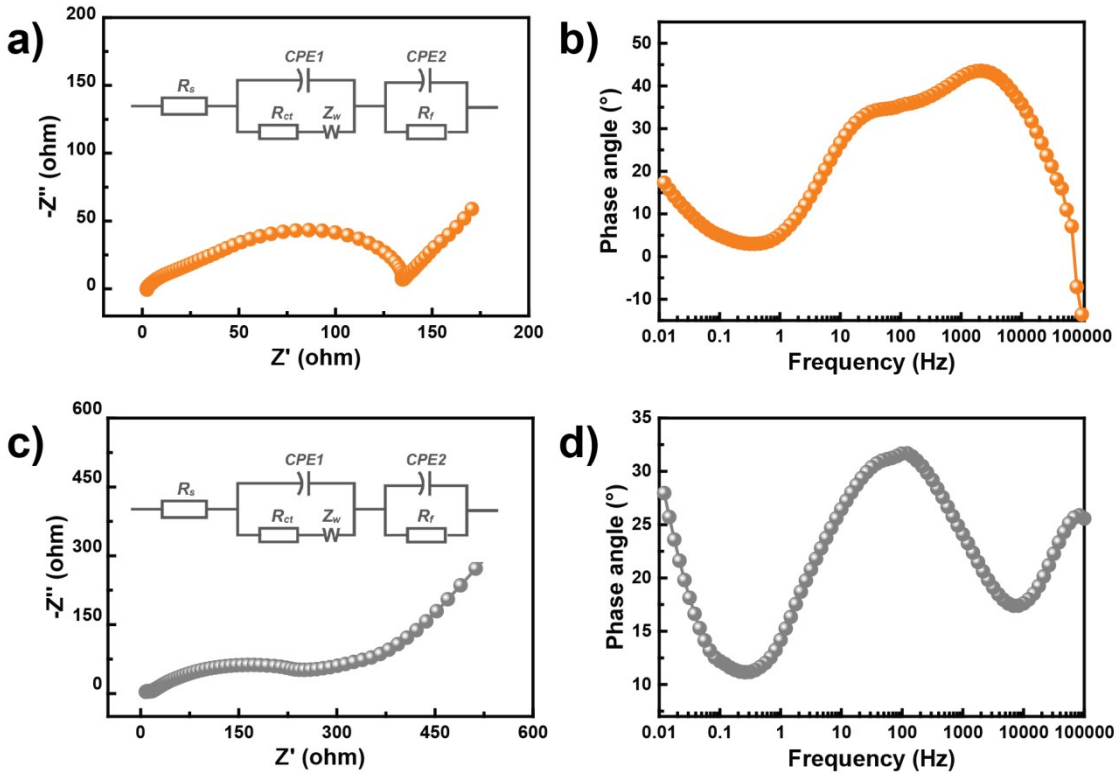

Fig. S18 The Nyquist and Bode phase angle plot of Zn//$V_3CrC_3T_x$ SCs a, b) and MSCs c, d), respectively.

Equation S1:

The ion diffusion coefficients (D_{ion}) of $V_3CrC_3T_x$ sample can be calculated based on the Randles Sevcik equation:

$$I_p = 2.69\times10^5 n^{3/2} S C_0^* D^{1/2} v^{1/2}$$

where I_p is the peak current, n is the number of electrons perspecies reaction (for Zn^{2+}, $n = 2$), S is the area of the electrode (1.13 cm^2), C_0^* is the concentration of zinc ions in the electrolyte (3 M), D is the ion diffusion coefficient, and v is the scanning rate.

Equation S2:

The ion diffusion coefficients of $V_3CrC_3T_x$ sample measured by EIS can be calculated based on the equation as follow:

$$D = R^2T^2 / 2n^4F^4A^2C^2\sigma^2$$

where R, T, A, F, and C corresponding to the gas constant, the absolute temperature, the area of electrode, the Faraday constant, and the molar concentration of ions, respectively. And σ is the Warburg coefficient, which can be calculated by plotting Z′ versus $\omega^{-1/2}$.

Equation S3:

The ion diffusion coefficients of $V_3CrC_3T_x$ sample measured by GITT can be calculated based on the equation as follow:

$$D^{GITT} = (4/\pi\tau)(m_B V_M / M_B S)^2 (\Delta E_s / \Delta E_\tau)^2$$

where τ is the constant current pulse time, m_B, V_M, S, and M_B are the mass, molar volume, area of the electrode, and molar mass of $V_3CrC_3T_x$ samples, respectively. ΔE_s is the voltage difference during the open circuit period, and ΔE_τ is the total change of cell voltage during a constant current pulse excluding the *IR* drop.

Equation S4:

The evaluation of the performance of flexible devices (f_d) can be described as follow:

$$f_d = \varepsilon E_v = (h/2r)(CV/A)/2r = 1/2(E_a/r)$$

where ε, E_v and E_a are the greatest tensile strain, volumetric energy density and areal energy density, respectively; C, V and A are the capacitance, nominal voltage, and area of the electrode, respectively.

Note:

As for an asymmetric supercapacitors device, it is well-known that the charge balance can be following the relationship $Q_+ = Q_-$, where Q_+ is the charges stored at the positive and

Q_- is the charges stored at the negative electrodes. The charge storage by each electrode depends on the specific capacitance (C_M), the potential range for the charge/discharge process (ΔE) and the effective mass of the electrode (M). The charge can be following equations:[1, 2]

$$Q = C_M \times \Delta E \times M$$

Besides, the specific capacitance of Vanadium-based MXene and Zn metal are ~1000 mAh g^{-1} and 823 mAh g^{-1}, respectively.[3, 4] And then, the ΔE_+ (0.6 V) and ΔE_- (0.75 V) can be obtained from relevant literatures.[5, 6] In order to obtain $Q_+ = Q_-$, the mass balance will be expressed as follows:

$$\frac{M_+}{M_-} = \frac{C_{M-}\Delta E_-}{C_{M+}\Delta E_+} = \frac{1.03}{1} \qquad (1\ \text{mAh g}^{-1} = 1\ \text{F g}^{-1} \cdot \frac{3.6}{\Delta E})$$

Normally, to compensate the consumption of zinc metal by the side reaction, the mass of the zinc metal anode is slightly excessive (more than 1:1.03, M_-:M_+), thus ensuring complete reaction of the cathode active material.[7, 8]

References:

1. N. Yu, K. Guo, W. Zhang, X. Wang and M.-Q. Zhu, *Journal of Materials Chemistry A*, 2017, **5**, 804-813.
2. S. Manoharan, D. Kesavan, P. Pazhamalai, K. Krishnamoorthy and S.-J. Kim, *Materials Chemistry Frontiers*, 2021, **5**, 2303-2312.
3. C. Wang, H. Xie, S. Chen, B. Ge, D. Liu, C. Wu, W. Xu, W. Chu, G. Babu, P. M. Ajayan and L. Song, *Advanced Materials*, 2018, **30**, 1802525.
4. L. Ma, Q. Li, Y. Ying, F. Ma, S. Chen, Y. Li, H. Huang and C. Zhi, *Advanced Materials*, 2021, **33**, 2007406.
5. S. Li, Q. Shi, Y. Li, J. Yang, T.H. Chang, J. Jiang and P.Y. Chen, *Advanced Functional Materials*, 2020, **30**, 2003721.
6. P. Zhang, Y. Li, G. Wang, F. Wang, S. Yang, F. Zhu, X. Zhuang, O. G. Schmidt and X. Feng, *Advanced Materials*, 2019, **31**, 1806005.
7. L. Ma, S. Chen, N. Li, Z. Liu, Z. Tang, J. A. Zapien, S. Chen, J. Fan and C. Zhi, *Advanced Materials*, 2020, **32**, 1908121.
8. J. Yang, B. Yin, Y. Sun, H. Pan, W. Sun, B. Jia, S. Zhang and T. Ma, *Nano-Micro Letters*, 2022, **14**, 42.

Table S1. The electrode materials and electrolytes of different flexible MSCs and their electrochemical performances.

Electrodes	Electrolytes	Voltage windows (V)	Areal capacitance (mF cm^{-2})	Areal energy density (μWh cm^{-2})	Ref.
$V_4CrC_3T_x$//Zn	PVA/$ZnSO_4$	0.15-1.3	278.3	51.12	**This work**
$Ti_3C_2T_x$/BCF// $Ti_3C_2T_x$/BCF	PAM/$Zn(CF_3SO_3)_2$	0-1.2	178.6	34.0	27
$Ti_3C_2T_x$//$Ti_3C_2T_x$ (IP&EP)	PVA/H_2SO_4	0-0.5	43	0.32	40
$Ti_3C_2T_x$//$Ti_3C_2T_x$ (LE)	PVA/H_2SO_4	0-0.6	27.3	1.3	41
$Ti_3C_2T_x$//$Ti_3C_2T_x$ (SP)	PVA/H_2SO_4	0-0.6	158	1.64	42
Be^{2+}-$Ti_3C_2T_x$//Be^{2+}-$Ti_3C_2T_x$	Gelatin/$ZnSO_4$	0-0.6	77.2	3.86	43
$Ti_3C_2T_x$//$Ti_3C_2T_x$ (Stamping)	PVA/H_2SO_4	0-0.6	56.8	0.76	44
$Ti_3C_2T_x$/BC// $Ti_3C_2T_x$/BC	PVA/H_2SO_4	0-0.6	112.2	5.54	45
$Ti_3C_2T_x$//Co-Al-LDH	PVA/KOH	0.4-1.45	40	8.84	46
MnO_2//Ppy	CMC/Na_2SO_4	0-1.5	25.8	0.51	17
RuO_2//RuO_2	PVA/H_2SO_4	0-1.0	27	3.1	47
Mn/Mo oxide//Mn/Mo oxide	PMMA/LiTFSI	0-0.8	7.5	4.2	48
Graphene//Graphene	PVA/H_3PO_4	0-0.8	0.62	1.3	18
MWCNT/PANI//MWCNT/PANI	PMMA/$LiClO_4$	0-0.8	44.13	3.92	49
P-Graphene//P-Graphene	PVA/KOH	0-1.5	21.7	5.9	50

Notes: Inkjet printing (IP), Extrusion printing (EP), Laser etching (LE), Screen printing (SP)